Acta Mech 223, 891–909 (2012)
DOI 10.1007/s00707-011-0610-z

Ryoichi Chiba · Yoshihiro Sugano

Optimisation of material composition of functionally graded materials based on multiscale thermoelastic analysis

Received: 2 September 2011 / Published online: 2 February 2012

Abstract This paper presents a method for optimisation of the material composition of functionally graded materials (FGMs) for thermal stress relaxation. This method consists of a multiscale thermoelastic analysis and a genetic algorithm. In the presented method, location-dependent unit cells representing the microstructures of two-phase FGMs are created using morphology description functions, and the homogenised material properties and microscale thermal stresses are computed using the asymptotic expansion homogenisation method. Thermal stress relaxation effects at the microscale in the FGMs are quantitatively evaluated, being reflected for the optimisation computation of the material composition. Numerical calculations are performed for a functionally graded infinite plate subjected to prescribed surface temperatures, and it is demonstrated that the optimisation with the knowledge of specific microstresses in FGMs results in not only a different trend of material composition distribution but also a different critical location for material failure from those obtained by conventional optimisation without the knowledge of the microstresses.

1 Introduction

Functionally graded materials (FGMs) are advanced composite materials formed of two or more constituents with a continuously variable composition. The varying material composition produces useful functions such as thermal stress relaxation, biological compatibility and refractive index control [1]. FGMs were originally developed to serve as high-performance heat resistant materials that can withstand large temperature gradients. Generally, this type of FGM is composed of a ceramic and a metal. In the present paper, we refer to this type of FGM as a 'FGM for thermal stress relaxation'.

The microstructure of a typical FGM for thermal stress relaxation is shown in Fig. 1 [2]. As shown in this figure, FGMs for thermal stress relaxation are both macroscopically and microscopically heterogeneous. Such two-phase FGMs make a transition from a particle-matrix microstructure, in which isolated particles are scattered within a matrix phase, to another particle-matrix microstructure via an interpenetrating network (or skeletal) structure, in which the two phases intertwine with each other, as the content of the second phase increases [1].

FGMs are referred to as 'designable materials'. In order to exploit the full potential of FGMs, they need to be fabricated according to the optimal material composition distribution that is predetermined in response to the

R. Chiba (✉)
Department of Mechanical Systems Engineering, Asahikawa National College of Technology,
2-2-1-6 Shunkodai, Asahikawa 071-8142, Japan
E-mail: chiba@asahikawa-nct.ac.jp
Tel.: +81-166-55-8003
Fax: +81-166-55-8003

Y. Sugano
Department of Mechanical Systems Engineering, Iwate University, 4-3-5 Ueda, Morioka 020-8551, Japan

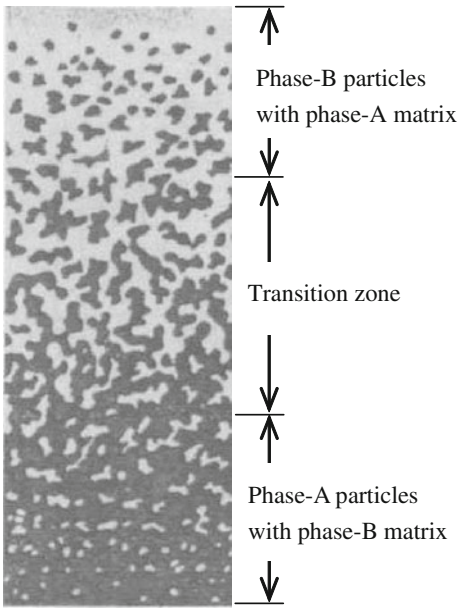

Fig. 1 Schematic illustration of the microstructural transition in a ceramic/metal FGM

environment in which they are used. In the case of FGMs for thermal stress relaxation, there are two prerequisites to the determination of their optimum material composition distribution: (i) accurate estimation methods for the effective thermomechanical properties and (ii) analytical techniques for solving heat conduction and thermoelastic problems of heterogeneous bodies with an arbitrary heterogeneity.

For an accurate estimation of the effective (or homogenised) material properties, information about the material composition and the microstructural morphology, which can greatly influence the material properties, must be taken into account. Higher-order techniques for the theoretical prediction of effective physical properties are continually being developed and a related review article has been published [3]. In existing studies focusing on the optimisation of the material composition distribution of FGMs, however, mean-field homogenisation techniques that assume simple microstructures (e.g. spherical inclusions dispersed in a matrix) have been employed [4–7] to estimate the effective material properties of FGMs. In other words, specific information regarding the microstructural morphology was neglected during these homogenisation calculations. Thus, the validity of the resultant optimum material composition distribution is disputable.

In the material design of FGMs for thermal stress relaxation, the objective of heat conduction and thermoelastic analyses is to quantitatively predict the distribution of thermal stresses in a functionally graded component under a given thermal loading condition. This allows us to assess the safeness of the component in the context of failure criteria for the FGMs. However, the relationship between the effective failure criteria (i.e. homogenised strength properties) at the macroscale in the FGMs and material composition (or microstructure) is not simple; this relationship is known to show a complicated variation in the transition zone (see Fig. 1) [2]. Moreover, coupled with the fact that an FGM for thermal stress relaxation is a composite material composed generally of a ductile material and a brittle material, micromechanics models that can estimate the effective failure criteria from the material composition and microstructure have not yet been established. For these reasons, reliable failure criteria based on the macroscopic stress state of FGMs have yet to be reported. Hence, the knowledge of macroscopic stress states obtained from conventional (macroscale) thermoelastic analyses alone is not sufficient to assess the safeness of functionally graded components. A solution to this issue is to evaluate the stress state at the microscale (i.e. microstress field), at which respective constituent materials are in a mixed state. With knowledge of the microstresses, one can apply material phase-specific failure criteria to better assess the failure of the heterogeneous material of the functionally graded component [8].

Existing studies on the microscale thermoelastic analysis of FGMs are limited. Pindera et al. [9] investigated the effects of microstructural architectures in graded thermal barrier coatings on thermal stress distributions using artificial material models with different levels of functionally graded microstructural refinement and different arrangements. Dao et al. [10] developed a computational micromechanics model to study the influences of discrete microstructure on residual stress distributions at the grain size level in FGMs. Tsukamoto [11] analysed microstresses in FGMs on the basis of Eshelby's equivalent inclusion method and Mori-Tanaka's

mean-field approximation; however, because this analysis evaluates volumetric average stresses in the matrix and dispersion phases, it cannot evaluate specific microstress distributions. Khan et al. [12] performed coupled heat conduction and deformation analyses of viscoelastic FGMs using a simplified micromechanical model for particle reinforced composites; unfortunately, their micromechanical model also failed to incorporate the effect of stress concentration at the microscale. Note that these four studies did not consider the FGM microstructural morphology. In contrast, Cannillo et al. [13] mapped SEM images of real FGM microstructures onto finite element meshes and numerically predicted the microscale thermal residual stresses that may arise during an FGM fabrication process. Similarly, Vena [14] analysed thermal residual stresses at the microscale in an FGM using a hybrid finite element approach, which takes account of the shape of the constituent material grains. However, analyses with full microscale models such as these are extremely time-consuming, and therefore, it is impractical to incorporate them into the computation of the optimal material composition.

The asymptotic expansion homogenisation (AEH) method is one of the multiscale analysis methods that can efficiently predict the microscopic stress state. It is a mathematically rigorous theory that includes the coupling between the macroscale and microscale and has received much attention in recent years [15]. The AEH method has the advantages that the equivalent macroscopic material properties for composite materials with an arbitrary complicated microstructure can be calculated exactly and the distribution of stresses in the microstructure can also be evaluated. The former advantage enables us to investigate the effects of microstructural morphology on the effective material properties in FGMs. In relation to this, a design methodology based on the AEH method for graded microstructures of functional materials has been proposed by Takano et al. [16]. Goupee et al. [8] first succeeded in applying the AEH method coupled with the finite element method (FEM) to the multiscale thermoelastic analysis of two-phase FGMs. They conducted a direct micromechanical failure analysis based on microstresses obtained from the multiscale analysis using numerically created microstructure models.

In the present study, an optimisation methodology is presented for the material composition distribution of FGMs for thermal stress relaxation. The methodology consists of a multiscale thermoelastic analysis by the AEH method and a genetic algorithm (GA). In the multiscale thermoelastic analysis, we use numerically created morphology models that describe the microstructures of the FGMs and the AEH method quantitatively evaluates local thermal stress concentrations induced by the microstructural heterogeneities. The quantified thermal stress relaxation effects at the microscale level are reflected for the optimisation computation of the material composition. For comparison purposes, we have also performed the conventional optimisation of material composition using simple mean-field homogenisation techniques [17], which does not require the computation of the microscopic stress states. The effects of the presence or absence of information about microstructural morphology and microstresses on the obtained optimum material composition distribution are investigated through a model problem for a functionally graded infinite plate subjected to prescribed surface temperatures.

2 Multiscale analysis of heat conduction and thermoelastic problems

This section contains a brief outline of the multiscale formulation of the steady heat conduction and thermoelastic problems using the AEH method. For more details, see [8], [15], and [16]. Note that the Einstein summation convention is used in the following formulation.

2.1 Heat conduction problem

Consider a two-phase functionally graded body with spatially varying microstructure, as shown in Fig. 2. A micro region in the macroscopic domain Ω is assumed to consist of a large number of microstructures that correspond to the macroscopic location, and the unit microstructure is referred to as a representative material element (RME), which occupies the domain Y. We assume a macroscale $\mathbf{x} \in \Omega$ and microscale $\mathbf{y} \in Y$ as shown in Fig. 2. Given that the characteristic lengths of the macroscopic body and RME are L and l, respectively, the ratio of the length scales is $\varepsilon = l/L \ll 1$ and the relationship between both scales is given by

$$\mathbf{y} = \frac{\mathbf{x}}{\varepsilon}. \tag{1}$$

For the steady heat conduction problem, the weak form of the governing equation is obtained by considering the effects of the microstructure as

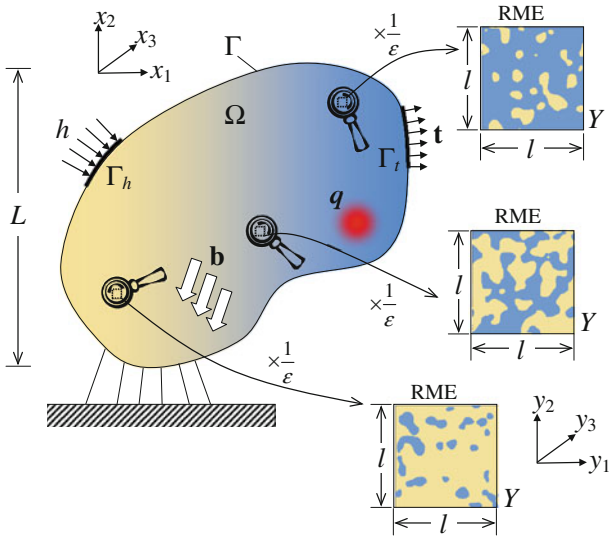

Fig. 2 Schematic of a two-phase functionally graded body with a microscale (y_i) and macroscale (x_i) coordinate system

$$\int_{\Omega} K_{ij} \frac{\partial T}{\partial x_j} \frac{\partial w}{\partial x_i} \mathrm{d}\Omega = \int_{\Omega} q w \mathrm{d}\Omega + \int_{\Gamma_h} h w \mathrm{d}\Gamma \quad \forall w(\mathbf{x}, \mathbf{y}), \tag{2}$$

where K_{ij} is the thermal conductivity tensor, w is a test function, and q and h denote the internal heat generation and the heat flux prescribed normal to the boundary Γ_h, respectively. K_{ij} reflects the microscopic heterogeneity represented by periodic functions.

The temperature is approximated with an asymptotic series representation in ε given by

$$T(\mathbf{x}, \mathbf{y}) = T^0(\mathbf{x}) + \varepsilon T^1(\mathbf{x}, \mathbf{y}) + \varepsilon^2 T^2(\mathbf{x}, \mathbf{y}) + \cdots, \tag{3}$$

where T^0 is the macroscopic (or homogenised) temperature and $T^n (n > 0)$ are the periodic temperatures in more refined scales. It has already been proven that macroscopic quantities such as T^0 are functions of macroscopic coordinates $\mathbf{x}$ only. We substitute Eq. (3) into Eq. (2) and neglect high-order terms ($O(\varepsilon^2)$). Subsequently, by using the following averaging principle for a periodic function $\Psi(\mathbf{y})$

$$\lim_{\varepsilon \to 0} \int_{\Omega} \Psi\left(\frac{\mathbf{x}}{\varepsilon}\right) \mathrm{d}\Omega = \int_{\Omega} \frac{1}{|Y|} \int_{Y} \Psi(\mathbf{y}) \mathrm{d}Y \mathrm{d}\Omega, \tag{4}$$

the coupled micro-macro problem can be decoupled into separate microscopic and macroscopic problems. Note that $|Y|$ represents the volume of the RME. The weak forms of the microscopic and macroscopic governing equations are, respectively:

$$\int_{Y} K_{ip} \frac{\partial \varphi^j}{\partial y_p} \frac{\partial w}{\partial y_i} \mathrm{d}Y = \int_{Y} K_{ij} \frac{\partial w}{\partial y_i} \mathrm{d}Y \quad \forall w(\mathbf{y}), \tag{5}$$

$$\int_{\Omega} K^{\mathrm{H}}_{ij} \frac{\partial T^0}{\partial x_j} \frac{\partial w}{\partial x_i} \mathrm{d}\Omega = \int_{\Omega} q^{\mathrm{H}} w \mathrm{d}\Omega + \int_{\Gamma_h} h w \mathrm{d}\Gamma \quad \forall w(\mathbf{x}). \tag{6}$$

By solving the microscopic equation, Eq. (5), under periodic boundary conditions over the RME domain Y, we can obtain the characteristic temperature functions $\varphi^j (j = 1, 2, 3)$, which depend only on the heterogeneity in the RME and the thermal conductivity tensors of the constituents. In Eq. (6), K^{H}_{ij} is the homogenised thermal conductivity tensor and q^{H} is the homogenised internal heat generation; these homogenised quantities are defined as

$$K_{ij}^{\mathrm{H}} = \frac{1}{|Y|}\int_Y \left(K_{ij} - K_{ip}\frac{\partial \varphi^j}{\partial y_p}\right) \mathrm{d}Y, \tag{7}$$

$$q^{\mathrm{H}} = \frac{1}{|Y|}\int_Y f \mathrm{d}Y. \tag{8}$$

2.2 Thermoelastic problem

For the thermoelastic problem, the weak form of the governing equation can be described by

$$\int_\Omega C_{ijkl}\frac{\partial u_k}{\partial x_l}\frac{\partial v_i}{\partial x_j}\mathrm{d}\Omega = \int_\Omega b_i v_i \mathrm{d}\Omega + \int_{\Gamma_t} t_i v_i \mathrm{d}\Gamma + \int_\Omega C_{ijkl}\alpha_{kl}(T - T_0)\frac{\partial v_i}{\partial x_j}\mathrm{d}\Omega \quad \forall v_i(\mathbf{x}, \mathbf{y}), \tag{9}$$

where C_{ijkl} is the elastic tensor, u_k is the displacement, v_i is a test vector (or an arbitrary virtual displacement), b_i and t_i denote the body force and the traction applied on the boundary Γ_t, respectively, and α_{kl} is the coefficient of thermal expansion (CTE). C_{ijkl} reflects the microscopic heterogeneity represented by periodic functions. T_0 is the initial temperature.

In the same way as the temperature field in the heat conduction problem, the displacement is expressed using the asymptotic expansion method as

$$u_i(\mathbf{x}, \mathbf{y}) = u_i^0(\mathbf{x}) + \varepsilon u_i^1(\mathbf{x}, \mathbf{y}) + \varepsilon^2 u_i^2(\mathbf{x}, \mathbf{y}) + \cdots, \tag{10}$$

where u_i^0 is the macroscopic (or homogenised) displacement and $u_i^n (n > 0)$ are the periodic displacements in more refined scales. By substituting Eqs. (3) and (10) into the governing equation, Eq. (9), and using the averaging principle given by Eq. (4), the coupled micro-macro problem can be decoupled into separate microscopic and macroscopic problems. The weak forms of the microscopic and macroscopic governing equations are:

$$\int_Y C_{ijmn}\frac{\partial \chi_m^{kl}}{\partial y_n}\frac{\partial v_i}{\partial y_j}\mathrm{d}Y = \int_Y C_{ijkl}\frac{\partial v_i}{\partial y_j}\mathrm{d}Y \quad \forall v_i(\mathbf{y}), \tag{11}$$

$$\int_Y C_{ijkl}\frac{\partial \psi_k}{\partial y_l}\frac{\partial v_i}{\partial y_j}\mathrm{d}Y = \int_Y C_{ijkl}\alpha_{kl}\frac{\partial v_i}{\partial y_j}\mathrm{d}Y \quad \forall v_i(\mathbf{y}), \tag{12}$$

$$\int_\Omega C_{ijkl}^{\mathrm{H}}\frac{\partial u_k^0}{\partial x_l}\frac{\partial v_i}{\partial x_j}\mathrm{d}\Omega = \int_\Omega b_i^{\mathrm{H}} v_i \mathrm{d}\Omega + \int_{\Gamma_t} t_i v_i \mathrm{d}\Gamma + \int_\Omega C_{ijkl}^{\mathrm{H}}\alpha_{kl}^{\mathrm{H}}(T^0 - T_0)\frac{\partial v_i}{\partial x_j}\mathrm{d}\Omega \quad \forall v_i(\mathbf{x}). \tag{13}$$

One of the microscopic equations, Eq. (11), provides the characteristic displacement functions χ_m^{kl}, which depend on the heterogeneity in the RME and the elastic tensors of the constituents. The other microscopic equation, Eq. (12), provides the characteristic displacement functions ψ_k associated with the heterogeneity and the CTEs of the constituents. In Eq. (13), C_{ijkl}^{H} is the homogenised elastic tensor, α_{ij}^{H} is the homogenised CTE and b_i^{H} is the homogenised body force. These are expressed as follows:

$$C_{ijkl}^{\mathrm{H}} = \frac{1}{|Y|}\int_Y \left(C_{ijkl} - C_{ijmn}\frac{\partial \chi_m^{kl}}{\partial y_n}\right)\mathrm{d}Y, \tag{14}$$

$$\alpha_{ij}^{\mathrm{H}} = \frac{D_{ijpq}^{\mathrm{H}}}{|Y|}\int_Y C_{pqkl}\left(\alpha_{kl} - \frac{\partial \psi_k}{\partial y_l}\right)\mathrm{d}Y, \tag{15}$$

$$b_i^{\mathrm{H}} = \frac{1}{|Y|}\int_Y b_i \mathrm{d}Y, \tag{16}$$

where D^{H}_{ijpq} denotes the homogenised compliance tensor, which is the inverse of the homogenised elastic tensor. The microscopic equations, Eqs. (11) and (12), are solved under periodic boundary conditions over the RME domain Y. To solve these equations for complex microstructures, a numerical method, e.g. the FEM, is generally required.

Once the macroscopic strains (=$(\partial u^0_k/\partial x_l + \partial u^0_l/\partial x_k)/2$) and macroscopic temperature T^0 are known, with the knowledge of χ^{kl}_m and ψ_k, the microstress components can be calculated as

$$\sigma_{ij} = \left(C_{ijkl} - C_{ijmn} \frac{\partial \chi^{kl}_m}{\partial y_n} \right) \frac{\partial u^0_k}{\partial x_l} - C_{ijkl} \left(\alpha_{kl} - \frac{\partial \psi_k}{\partial y_l} \right) (T^0 - T_0). \tag{17}$$

Obtaining homogenised quantities on the basis of microstructural information, as shown in Eqs. (7), (8) and (14–16), is referred to as a 'homogenisation process', whereas investigating the stress response of microstructures, as shown in Eq. (17), is referred to as a 'localisation process'.

3 Material structure modelling of FGMs

3.1 Macrostructure

For the optimisation of the material composition of FGMs for thermal stress relaxation, we consider a two-phase (ceramic/metal) FGM whose material properties vary only in one direction. The optimisation of the material composition distribution of a two-phase FGM is equivalent to the optimisation of the volume fraction distribution of one of its constituent phases. In order to facilitate the optimisation process with AEH-based multiscale analysis, we approximate the continuous volume fraction distribution function of the original FGM with a step function. The reason for this is that a direct point-wise optimisation of the volume fraction at every location along the graded direction is computationally expensive and therefore intractable. As a result, we have used a multi-layer description of the FGM, in which the microstructural morphology is uniform in each layer but is different from the microstructural morphology in neighbouring layers. Because of the multi-layer approximation, the overall FGM responses show zigzag variations (discontinuities) along the graded direction. However, the discontinuities in the FGM can be reduced by increasing the number of the fictitious layers, n, along the graded direction. Of course, this approximation is unnecessary for FGMs originally made of a series of layers with different material compositions.

3.2 Microstructure

The microstructural morphology for each fictitious layer is defined using a morphology description function (MDF). This approach was employed to design microstructures for functional porous materials [18] and to create realistic computational models of microstructures for FGMs [8,19,20]. In the latter case, depending on the choice of MDF, a wide variety of microstructural morphologies with desired phase volume fractions can be created. The variation in the microstructural morphologies along the graded direction over the macroscopic domain Ω is specified on the basis of the spatial variation in the phase volume fractions along the same direction; these variations are both stepwise in the present study.

4 Volume fraction optimisation using a genetic algorithm

4.1 Formulation of the optimisation problem

The optimisation of the material composition distribution of a two-phase FGM now reduces to determining the optimal volume fraction of one of the constituent phases in each layer of a multi-layer system. In this case, the optimisation problem with the necessary constraint conditions can be written in the following form:

$$\begin{array}{ll} \text{Design variables} & \mathbf{V}, \\ \text{Minimise} & f(\mathbf{V}), \\ \text{Subject to} & 0 \le V_i \le 1, i = 1, 2, \ldots, n, \\ & V_i \le V_{i+1}, i = 1, 2, \ldots, n-1, \end{array} \tag{18}$$

where $\mathbf{V} = [V_1, V_2, \ldots, V_n]$ is the vector of volume fractions in the respective layers and $f(\mathbf{V})$ is the objective function to be minimised. The specific form of $f(\mathbf{V})$ is discussed in the next subsection. The above optimisation problem includes n design variables.

4.2 Objective function

To construct an objective function for optimising the material composition distribution of FGMs for thermal stress relaxation, we consider a macroscopic safety index $g(\mathbf{x})$ based on a direct micromechanical failure analysis. A detailed description of the safety index is given in Appendix A. This safety index indicates how safe a composite material is at a point $\mathbf{x}$ and is determined by the relationship between the microstress field in the material and phase-specific failure criteria. This concept was first used for a direct micromechanical failure analysis of FGMs by Goupee et al. [8,19]; they introduced a 'factor of safety' therein. The safety index g used in the present study is equivalent to the inverse of the 'factor of safety'. In the present study, the maximum of the safety index g evaluated over the entire macroscopic domain Ω is considered as the objective function, i.e.

$$f(\mathbf{V}) = \max_{\mathbf{x}\in\Omega} g(\mathbf{x}). \tag{19}$$

4.3 Genetic algorithm

In order to solve the optimisation problem, we use a GA, which has the advantage of a rapid and efficient global searching ability, and can be applied to optimisation problems in which the gradient information is not available. GA is a biologically inspired optimisation method in which the population of candidate solutions evolves towards an optimal solution using genetic concepts. GAs were originally developed using binary-coded genetic strings. Subsequently, extended GAs coded using real valued parameters instead of binary strings (namely, real-coded GAs) have been proposed, being employed for optimisation in a continuous search space. In the present study, however, the former type (a discrete-coded type) of GA [21] is employed for conceptual simplicity. Since a number of books on GAs have been published, detailed descriptions of each stage (e.g. selection, crossover, mutation and scaling) of the GA procedure are omitted here.

The value of V_i in each layer is incorporated in a chromosome as a gene that comprises a 6-bit binary number (see Fig. 3). It should be noted that whenever new chromosomes are created during the evolution process, the volume fraction values in the layers are sorted in ascending order with increasing the layer numbers to meet the constraint conditions shown in Eq. (18). Each individual inherits one chromosome, which consists of n genes. In this case, each V_i can take 2^6 discrete values and therefore the size of the solution space is $2^6 \cdot (2^6 + 1) \ldots (2^6 + n - 1)/n!$ under the constraint conditions. Table 1 shows the specifications of the GA used for the optimisation. The fitness rating F to be used as a selection criterion for individuals to survive into the next generation is defined by

$$F = \frac{1}{f(\mathbf{V})}. \tag{20}$$

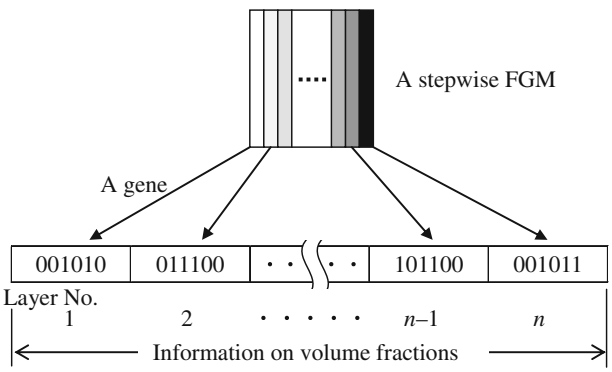

Fig. 3 Binary coding of volume fraction values of respective layers for an individual

Table 1 Specifications for GA optimisation procedure

Item	Adopted rule/value
Length of bit strings of an individual	60
Population size	40
Selection	Roulette wheel selection and elitism
Crossover/probability	Uniform crossover/0.75
Mutation/probability	One-point mutation/0.01
Scaling	power law scaling

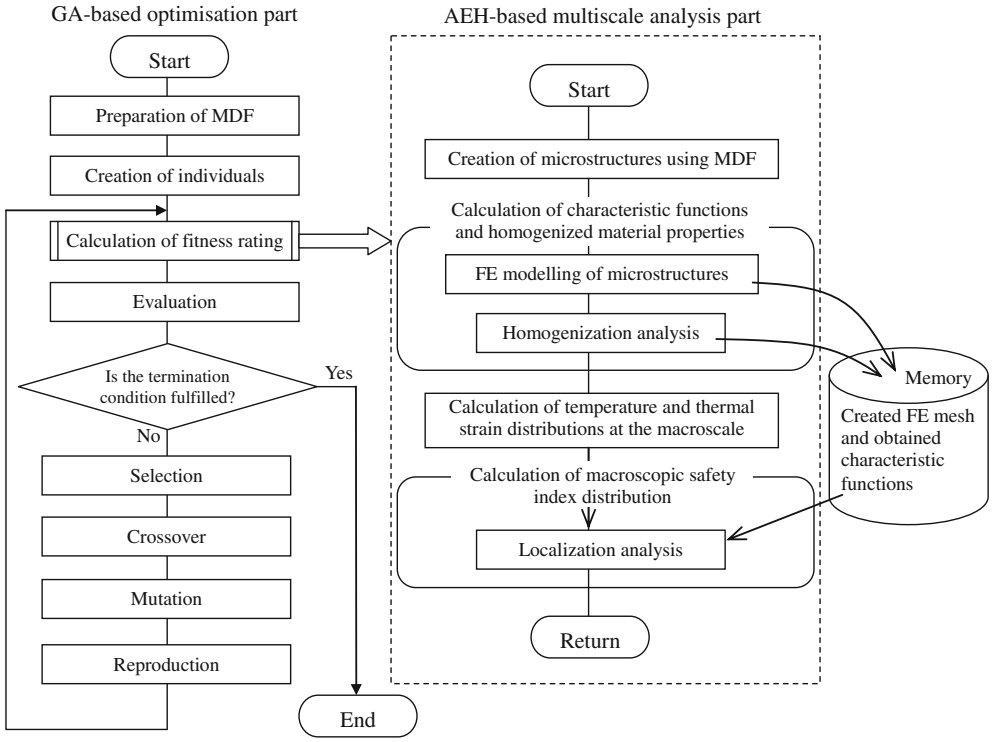

Fig. 4 Flow chart of GA optimisation procedure

The evolution process is iterated until the evolution for 10 generations does not change the best individual after the power-law scaling coefficient reaches 10. Figure 4 shows a flow chart of the optimisation process.

5 Validation of multiscale analysis

Prior to optimising the volume fraction distribution of FGMs for thermal stress relaxation, the multiscale analysis code that we developed was verified by comparing the results for the homogenised material properties obtained from our computation with the results presented in a previous study [8] for a Ti/ZrO_2 FGM plane-stress body with a realistic variation in the microstructure. The temperature-dependent material properties for the titanium and zirconia phases are given in Table 2 [8]. The microstructures of the Ti/ZrO_2 FGM across the entire range of volume fraction variations have been created using a MDF as follows [20]:

$$p(\mathbf{y}) = \sum_{i=1}^{N} c_i \exp\left\{-N\left[\frac{\left(y_1 - y_1^{(i)}\right)^2 + \left(y_2 - y_2^{(i)}\right)^2}{l^2}\right]\right\}, \tag{21}$$

where the coefficients $c_i \in [-1, 1]$ and $(y_1^{(i)}, y_2^{(i)}) \in Y$ are randomly chosen. Following Goupee et al. [8], $N = 800$ is adopted here to create the microstructures. The microscale analyses (to be exact, the homogenisation

Table 2 Temperature-dependent material properties of Titanium and Zirconia, T in Kelvin

Material property	Ti	ZrO_2
K (W/mK)	$1.1 + 0.017T$	$1.71 + 0.21 \times 10^{-3}T + 0.116 \times 10^{-6}T^2$
E (GPa)	$122.7 - 0.0565T$	$132.2 - 50.3 \times 10^{-3}T - 8.1 \times 10^{-6}T^2$
ν	$0.2888 + 32 \times 10^{-6}T$	0.333
α (1/K)	$7.43 \times 10^{-6} + 5.56 \times 10^{-9}T - 2.69 \times 10^{-12}T^2$	$13.31 \times 10^{-6} - 18.9 \times 10^{-9}T + 12.7 \times 10^{-12}T^2$
σ_y (MPa)	$1252.0 - 0.8486T$	–
σ_{ut} (MPa)	–	$148.1 + 1.184 \times 10^{-3}T - 31.4 \times 10^{-6}T^2$
σ_{uc} (MPa)	–	$3181.2 + 25.43 \times 10^{-3}T - 0.675 \times 10^{-3}T^2$

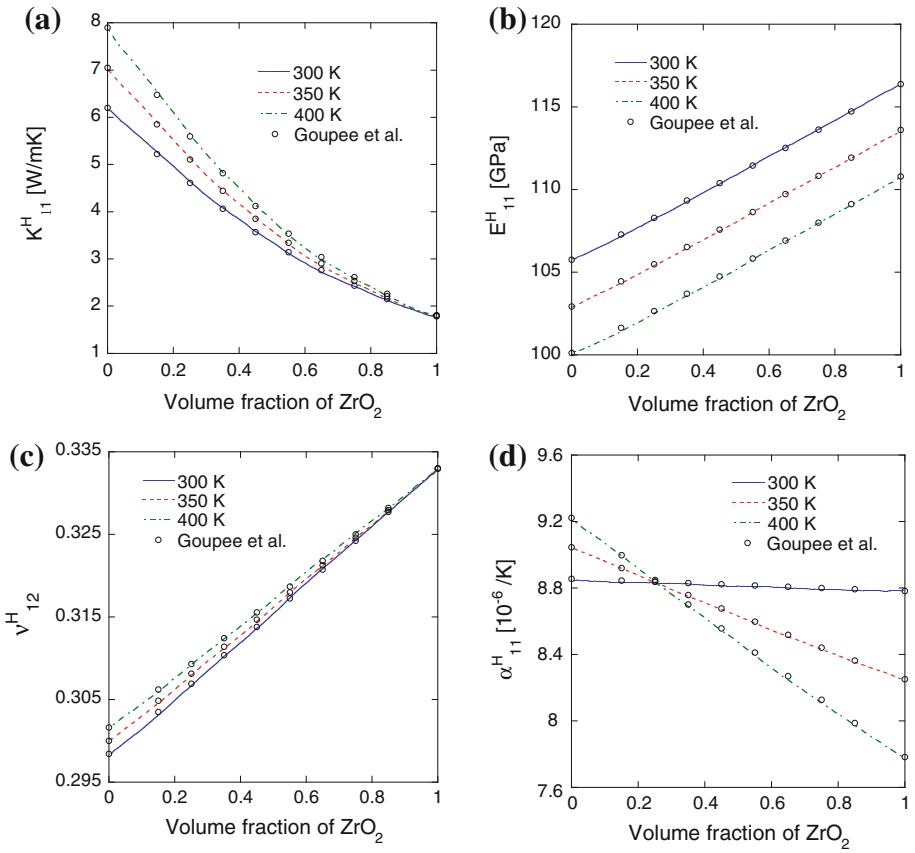

Fig. 5 Homogenised material properties at different volume fractions and temperatures: **a** thermal conductivity, **b** Young's modulus, **c** Poisson's ratio and **d** coefficient of thermal expansion

processes) are performed by the FEM. The FE mesh used was a regular mesh of 2,500 four-noded isoparametric quadrilateral elements.

The homogenised material properties for the Ti/ZrO_2 FGM with microstructures obtained from the MDF, Eq. (21), at three different temperatures are plotted in Fig. 5 as a function of the ZrO_2 volume fraction. There is a good agreement between our numerical results and the results of Goupee et al. [8] at all three temperatures. Hence, it has been demonstrated that the characteristic temperature functions (see Eq. (7)) and characteristic displacement functions (see Eqs. (14) and (15)), which are necessary to calculate the homogenised material properties, are correctly obtained thorough our multiscale analysis code. This implies that the microstresses computed via Eq. (17) including the characteristic functions are also correctly obtained through the multiscale analysis code.

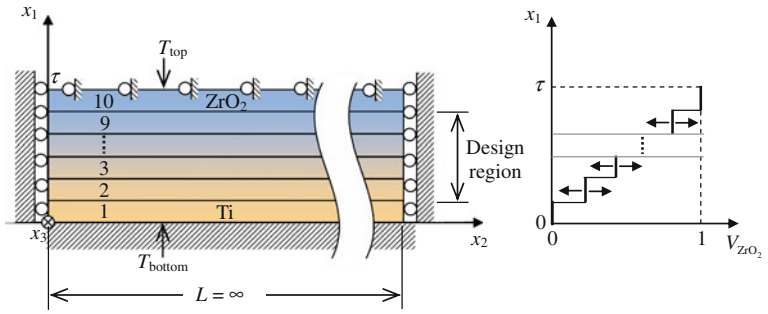

Fig. 6 Schematic of thermal loading, boundary conditions and volume fraction distribution for a Ti/ZrO_2 10-layered functionally graded infinite plate

6 Volume fraction optimisation of a functionally graded infinite plate

In this section, the proposed optimisation approach for the material composition distribution of FGMs for thermal stress relaxation is demonstrated via a model problem that necessitates a two-dimensional multiscale analysis. Consider a Ti/ZrO_2 functionally graded infinite plate with thickness τ in which the material composition varies only along the thickness direction. The functionally graded plate is approximated as an assembly of 10 layers with identical thickness, as shown schematically in Fig. 6. We define x_1 as the relative distance from the pure metal (Ti), i.e. $x_1 = 0$ stands for the pure Ti and $x_1 = \tau$ stands for the pure ceramic (ZrO_2). In order to simplify the multiscale analysis, the functionally graded plate is considered to be macroscopically transversely isotropic in the x_1–x_2 plane, similar to Shabana et al. [22]. In other words, the microstructures of the functionally graded plate do not vary along the x_3-direction in this model problem. For simplicity, it is assumed that the dependence of material properties on temperature is negligible and no heat is generated in the plate. The top and bottom surfaces of the plate are kept at $T_{top} = 500$ K and $T_{bottom} = 300$ K, respectively, and the heat is considered to flow along the x_1-direction only. Moreover, a plane-stress state in the thickness direction is assumed, and both in-plane and out-of-plane deformations of the plate are restricted. In this case, the macroscopic steady-state temperature, macroscopic stresses and strains (denoted by symbols with a bar) are obtained as follows:

$$T^0(x_1) = \frac{T_{top} - T_{bottom}}{\int_0^\tau \frac{1}{K_{11}^H(\xi)} d\xi} \int_0^{x_1} \frac{1}{K_{11}^H(\xi)} d\xi + T_{bottom}, \tag{22}$$

$$\bar{\sigma}_{11} = 0, \bar{\sigma}_{22}(x_1) = -\frac{E_{22}^H(x_1)\Delta T(x_1)}{1 - \nu_{32}^H(x_1)\nu_{23}^H(x_1)} \left[\alpha_{22}^H(x_1) + \nu_{23}^H(x_1)\alpha_{33}^H(x_1)\right],$$

$$\bar{\sigma}_{33}(x_1) = -\frac{E_{33}^H(x_1)\Delta T(x_1)}{1 - \nu_{23}^H(x_1)\nu_{32}^H(x_1)} \left[\alpha_{22}^H(x_1)\nu_{32}^H(x_1) + \alpha_{33}^H(x_1)\right], \tag{23}$$

$$\bar{\varepsilon}_{11}(x_1) = \frac{\Delta T(x_1)}{1 - \nu_{32}^H(x_1)\nu_{23}^H(x_1)} \left\{\nu_{12}^H(x_1)\left[\alpha_{22}^H(x_1) + \nu_{23}^H(x_1)\alpha_{33}^H(x_1)\right] + \nu_{13}^H(x_1)\left[\nu_{32}^H(x_1)\alpha_{22}^H(x_1) + \alpha_{33}^H(x_1)\right]\right\} + \alpha_{11}^H(x_1)\Delta T(x_1),$$

$$\bar{\varepsilon}_{22} = \bar{\varepsilon}_{33} = 0, \tag{24}$$

where E_{ij}^H is the homogenised Young's modulus, ν_{ij}^H is the homogenised Poisson's ratio, ΔT is the temperature rise from stress-free state ($=T^0 - T_{bottom}$), and the macroscopic shear stresses and shear strains are all zero.

Because the homogenised properties E_{33}^H, α_{33}^H, ν_{23}^H, ν_{32}^H, and ν_{13}^H in Eqs. (22)–(24) cannot be obtained from the homogenisation process by the two-dimensional AEH method, α_{33}^H is estimated by a combination of Schapery's axial CTE model [23] and fuzzy inference [24], and the remainder by the linear rule of mixtures. It is known that the longitudinal elastic properties of unidirectional fibrous composites follow the rule of mixtures very closely. The material properties of Ti and ZrO_2 at 400 K (see Table 2) are used in this computation.

Two types of microstructural morphology expressions are employed to create the microstructures of the functionally graded plate to be used for the model problem. One of the types of expressions describes

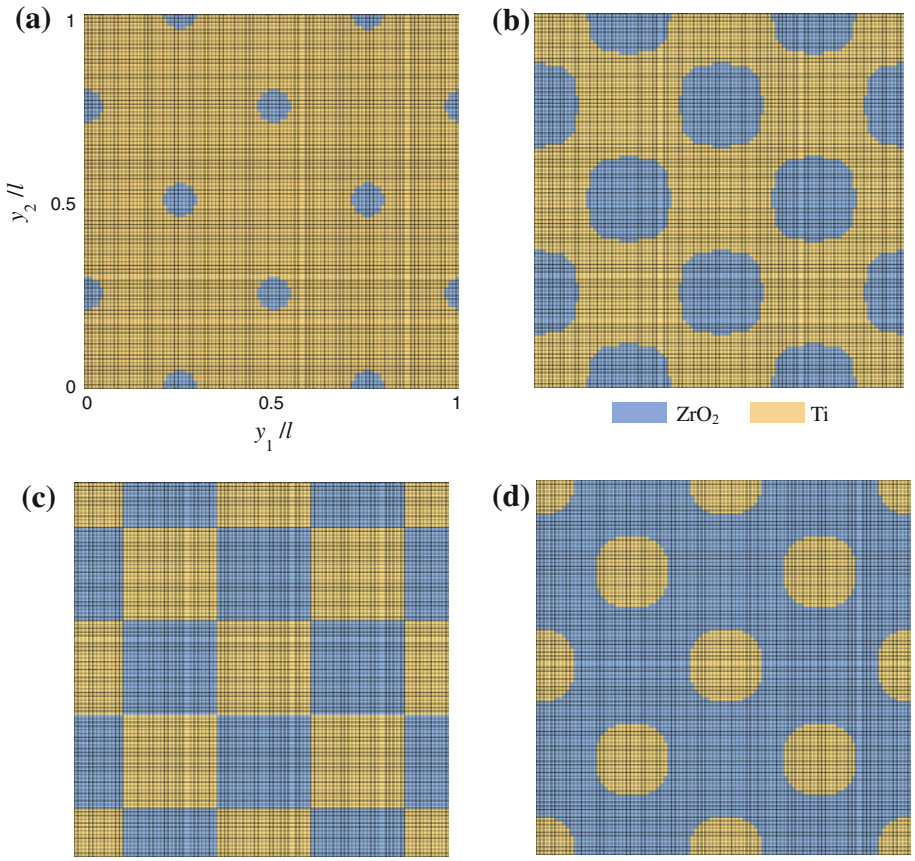

Fig. 7 Microstructural morphologies with finite element mesh for ZrO_2 volume fractions of **a** 0.05, **b** 0.35, **c** 0.50 and **d** 0.75

microstructural morphologies such that isolated inclusions are distributed in a matrix in a staggered arrangement; the following MDF has been employed to create these morphologies:

$$p(\mathbf{y}) = \frac{1}{4}\left[2 - \cos\left(2\pi \cdot \frac{y_1 + y_2}{l}\right) - \cos\left(2\pi \cdot \frac{y_1 - y_2}{l}\right)\right]. \tag{25}$$

The created microstructural morphologies corresponding to zirconia volume fractions of $V_{ZrO_2} = 0.05, 0.35, 0.50$, and 0.75 are displayed in a tiled 2×2 format in Fig. 7a–d, respectively. The staggered arrangement is known to be more representative of FGM microstructures that exhibit random inclusion distributions than a square array arrangement [9,25].

The other type of microstructural morphology expression describes realistic microstructural morphologies of FGMs for thermal stress relaxation; the microstructures of the functionally graded plate across the entire range of volume fraction variations have been created using Eq. (21) with $N = 800$. The representative microstructural morphologies created for several values of the volume fraction can be found in [8,20] and hence their presentation is omitted here. Because the microstructures generated by the random MDF, Eq. (21), for a sufficiently large value of N have been confirmed to be isotropic, the assumption that the functionally graded plate is macroscopically transversely isotropic is not violated. For both types of microstructural morphology expressions, the plane strain state is assumed at the microscale, and the microscopic problems are solved by the FEM with the aforementioned regular mesh.

Vel et al. [20] investigated the relationship between the fineness of the finite element mesh (comprised of six-noded triangular elements) and the resultant homogenised material properties for a composite material with an interpenetrating network-like microstructure (or skeletal microstructure) created by the random MDF, Eq. (21), with $N = 800$. They observed that the use of more than 3,200 elements provides calculated values for the homogenised material properties that have converged sufficiently. In addition, Goupee et al. [19] investigated the relationship between the mesh fineness and the calculated maximum microstress in the same

composite material, showing that more than 8,000 elements are needed to result in a sufficiently converged value for the microstress. Thus, the present finite element computation, which uses a regular mesh comprising 2,500 simple four-noded quadrilateral elements, may not yield highly accurate homogenised material properties and microstresses. However, considering the trade-off between the accuracy and the computational burden of the optimisation computation, we decided to use 2,500-elements.

In the optimisation process using the GA, we set $V_1 = 0$ and $V_{10} = 1$ and hence the volume fractions of only eight intermediate layers are design variables. Moreover, the value of g in Eq. (19) is evaluated at 11 discrete points along the graded direction with equal intervals in each layer, and the maximum of those evaluated in all the layers is taken as the value of f.

For comparison purposes, we also perform the conventional optimisation of the material composition using simple mean-field homogenisation techniques [17], which does not require the computation of the stress state at the microscale. 'Appendix B' describes our method of estimating the effective material properties of the FGM and also the objective function that was used for this optimisation.

7 Results and discussion

Figure 8 shows the optimised material composition distribution and the corresponding macroscopic/microscopic analysis results for the functionally graded plate with microstructures such that isolated inclusions are distributed in a matrix in a staggered arrangement. The through-the-thickness profile of a ZrO_2 volume fraction is given in Fig. 8a. As shown in the figure, this optimal volume fraction distribution is obtained by the GA evolution for 144 generations, and the final fitness rating, given by Eq. (20), is 4.8450. Note that the corresponding objective function value is the inverse of the fitness rating. A feature that the volume fraction increases rapidly on the heating side of the plate is observed. The through-the-thickness variations in the macroscopic temperature and thermal stresses are shown in Fig. 8b. There is no clear difference between $\bar{\sigma}_{22}$ and $\bar{\sigma}_{33}$ on this graph; the maximum difference is approximately 0.1%. Therefore, in the present numerical example, the functionally graded plate can be considered to be macroscopically isotropic. The macroscopic thermal stresses in the plate are compressive throughout the thickness, and their absolute values increase monotonically towards the heating surface of the plate. Figure 8c illustrates the distribution of a microstress in the RME at $x_1/\tau = 0.9$ belonging to the 9th layer, at which the largest value of the macroscopic safety index g (see Eq. (A1)) within the entire macroscopic domain of the functionally graded plate is observed. In this figure, element solutions obtained from the microscale analysis by the FEM are shown as a contour plot. Compared with the structure of the corresponding RME shown in Fig. 8e, it can be seen that large compressive stresses arise in the metal phase. Note that the areal mean of the stress value over the RME agrees with the value of $\bar{\sigma}_{22}$ at $x_1/\tau = 0.9$ (in the 9th layer) in Fig. 8b. Figure 8d is a contour plot of the microscopic safety index (see Eq. (A2)) in the same RME. Because of the symmetry of the microstructure, there are eight locations where the maximum value is observed. These locations are critical locations for material failure in the domain and all correspond to metal phase elements located at the boundaries between the metal phase and ceramic phases.

Figure 9 contains the optimised material composition distribution and corresponding macroscopic/microscopic analysis results for the functionally graded plate with realistic microstructures of FGMs for thermal stress relaxation. Compared with the through-the-thickness profile of the ZrO_2 volume fraction shown in Fig. 8a, while there is a discernible difference in the volume fraction of the 9th layer, it is similar in that the volume fraction increases rapidly on the heating side of the plate. Moreover, the fitness rating of this optimal volume fraction distribution is smaller than that shown in Fig. 8a. This indicates that the optimally designed FGM with realistic microstructures is more likely to cause material failure than its counterpart with simple microstructures. Furthermore, on optimising the material composition distribution of FGMs for thermal stress relaxation, which actually have complicated microstructures as shown in Fig. 1, assuming their microstructures as simple geometric (e.g. spherical) inclusions embedded in a matrix leads to a significant error: although the obtained material composition distribution may be close to that obtained from the optimisation without the assumption, the safety allowance of the FGM with the resultant optimised material composition distribution against thermal loading is overestimated. Figure 9b shows the corresponding through-the-thickness variations in the macroscopic temperature and thermal stresses. There is no significant difference between $\bar{\sigma}_{22}$ and $\bar{\sigma}_{33}$ in the case of the realistic microstructures either, and therefore, the functionally graded plate can be considered to be macroscopically isotropic. The macroscopic thermal stresses are also compressive throughout the thickness. Figure 9c is a contour plot of a microstress in the RME at $x_1/\tau = 0.9$ in the 9th layer, at which the largest value of the macroscopic safety index within the entire macroscopic domain of the functionally graded plate is

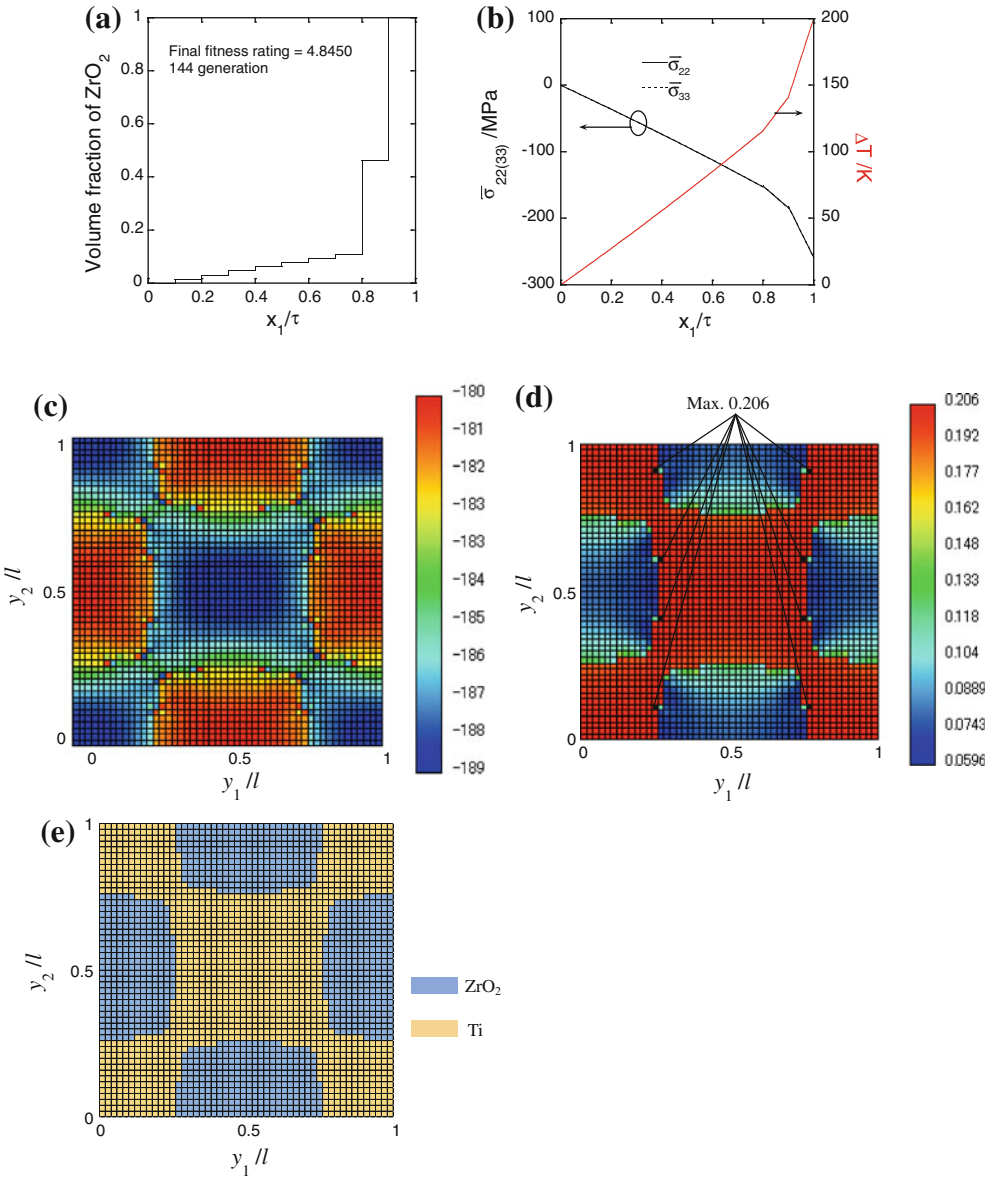

Fig. 8 **a** Optimised volume fraction distribution, **b** corresponding temperature and macrostress distributions, contour plots of **c** microstress σ_{22} in MPa and **d** microscopic safety index, G, over the microstructure at the critical location $x_1/\tau = 0.9$ in the 9th layer, and **e** microstructural morphology of the 9th layer, for a functionally graded plate with simple microstructures

observed, that is, the critical location for material failure. Compared with the microstructure shown in Fig. 9e, it is observed that the compressive stresses are large especially in the metal phases. The distribution of the microscopic safety index in the same RME is shown in Fig. 9d. One can see that the value tends to be high in metal phases and the maximum value is found at a metal phase element at a boundary between the metal and ceramic phases.

Figure 10 illustrates the material composition distribution of the functionally graded plate obtained from the conventional optimisation method using the simple mean-field homogenisation techniques and the corresponding macroscopic responses. In the obtained design proposal, the ZrO_2 volume fraction increases exponentially towards the heating surface, as shown in Fig. 10a. This is a different trend from the volume fraction distribution obtained through the optimisation computation based on the multiscale analysis (Figs. 8a, 9a). Owing to the difference in the objective functions used for the GA optimisations, the fitness rating for the obtained volume fraction distribution is considerably higher than those shown in Figs. 8a and 9a. Figure 10b shows

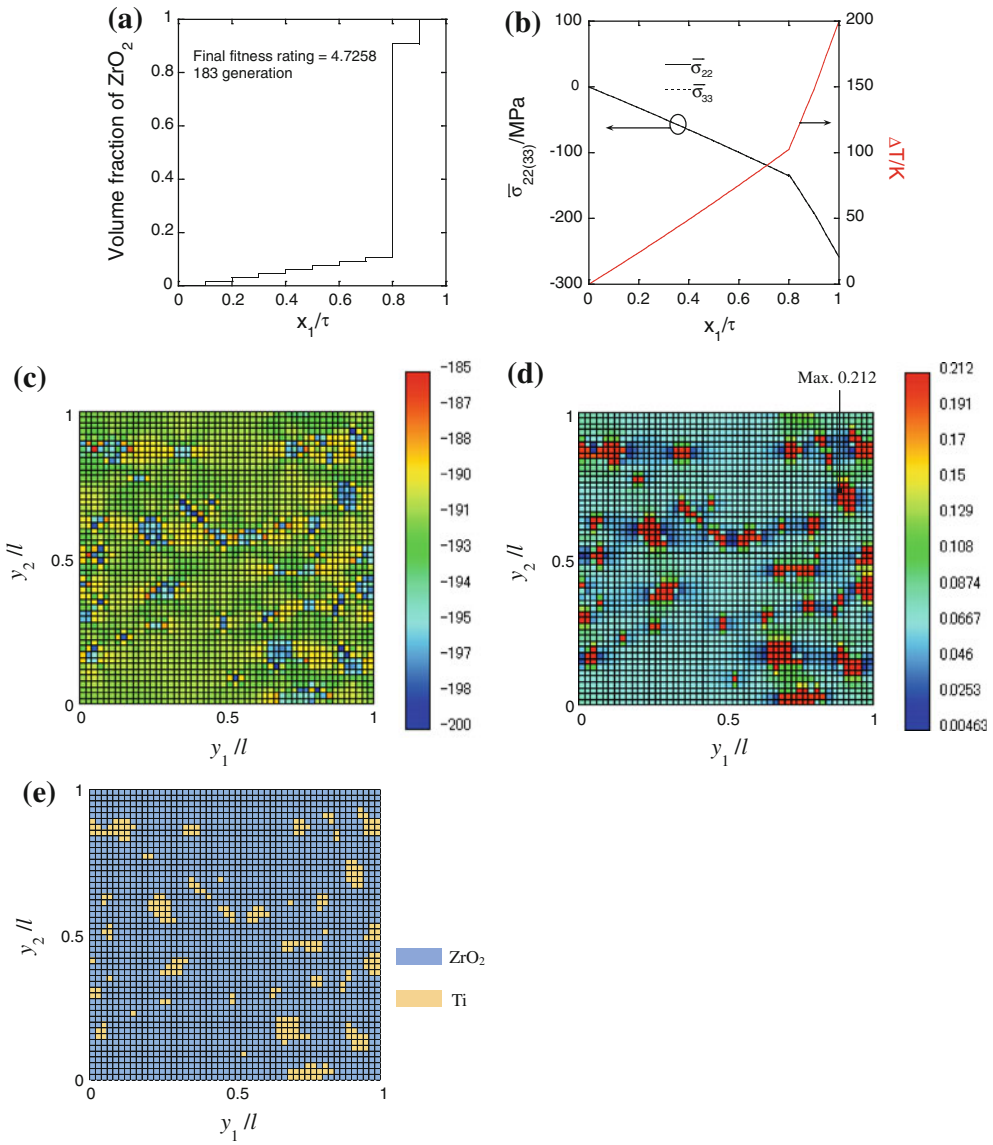

Fig. 9 **a** Optimised volume fraction distribution, **b** corresponding temperature and macrostress distributions, contour plots of **c** microstress σ_{22} in MPa and **d** microscopic safety index, G, over the microstructure at the critical location $x_1/\tau = 0.9$ in the 9th layer, and **e** microstructural morphology of the 9th layer, for a functionally graded plate with realistic microstructures

the through-the-thickness variations in the corresponding macroscopic temperature and thermal stresses. The functionally graded plate undergoes an equibiaxial compression in the x_2–x_3 plane, similarly to that shown in Figs. 8b and 9b. The through-the-thickness variation in the local safety factor calculated from Eq. (B2) is shown in Fig. 10c. The maximum value is observed at $x_1/\tau = 1$; this means that the material failure is most likely to occur at the heating surface. In summary, it has been demonstrated that optimisation with the knowledge of specific microstresses in FGMs results in not only a different trend of optimised material composition distribution but also a different critical location in terms of material failure from those obtained by optimisation without the knowledge of microstresses.

For confirmation, the multiscale analysis by the AEH method was conducted to investigate microstresses appearing in the functionally graded plate with the ZrO_2 volume fraction distribution shown in Fig. 10a, which contains realistic microstructures. Figure 11a, b shows microscopic thermal stress distributions within the RME at $x_1/\tau = 0.9$ in the 9th layer, at which the largest value of the macroscopic safety index throughout the entire macroscopic domain of the plate is observed. Since the RME exhibits an interpenetrating network structure (Fig. 11d), the stress distributions are rather complicated. However, it can be seen that large compressive

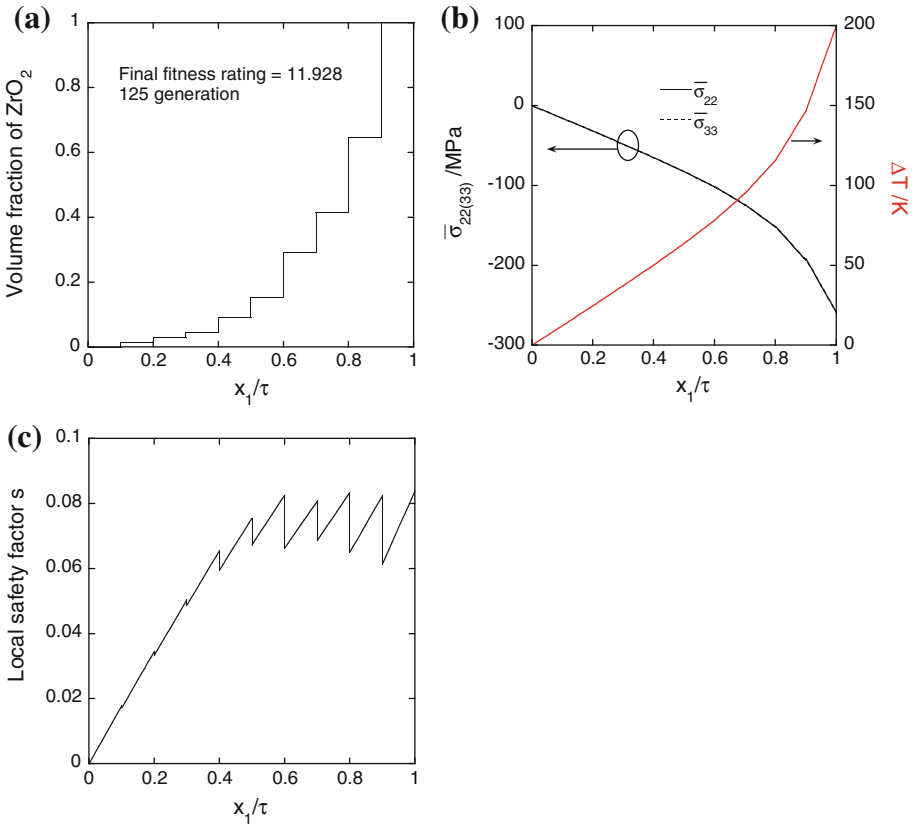

Fig. 10 **a** Volume fraction distribution obtained from the conventional optimisation procedure without the computation of microstresses, **b** corresponding temperature and macrostress distributions and **c** distribution of local safety factor, s, over the macroscopic domain of the functionally graded plate

stresses tend to occur in metal phases. Figure 11c is a contour plot of the microscopic safety index in the same RME. The maximum value of 0.224 is higher than that (0.212) for the functionally graded plate with the volume fraction distribution shown in Fig. 9a. Consequently, it has been confirmed that the volume fraction distribution shown in Fig. 10a (i.e. the material composition distribution obtained from the conventional optimisation method) is not optimum in terms of material failure at the microscale.

Finally, several computation runs were performed with different seeds to generate the random parameters c_i, $y_1^{(i)}$, and $y_2^{(i)} (i = 1, 2, \ldots, N)$ in Eq. (21), which are needed to create realistic FGM microstructural morphologies. We have verified that in all of the runs, the optimised ZrO_2 volume fraction distribution of the functionally graded plate with realistic microstructures is identical to the distribution shown in Fig. 9a and the volume fraction distribution shown in Fig. 10a never agrees with the optimum distribution in terms of material failure at the microscale.

8 Conclusions

In this study, an optimisation methodology has been presented for the material composition distribution of FGMs for thermal stress relaxation. The methodology consists of a multiscale thermoelastic analysis by the asymptotic expansion homogenisation method and a genetic algorithm. For FGMs with microstructures created using morphology description functions, the multiscale analysis including the homogenisation and localisation processes is conducted by the asymptotic expansion homogenisation method coupled with a finite element technique. Thermal stress relaxation effects at the microscale in FGMs are quantitatively evaluated, being reflected for the optimisation computation of the material composition. The functionally graded component under consideration is approximated as a multilayered body, and the volume fraction values of one of the

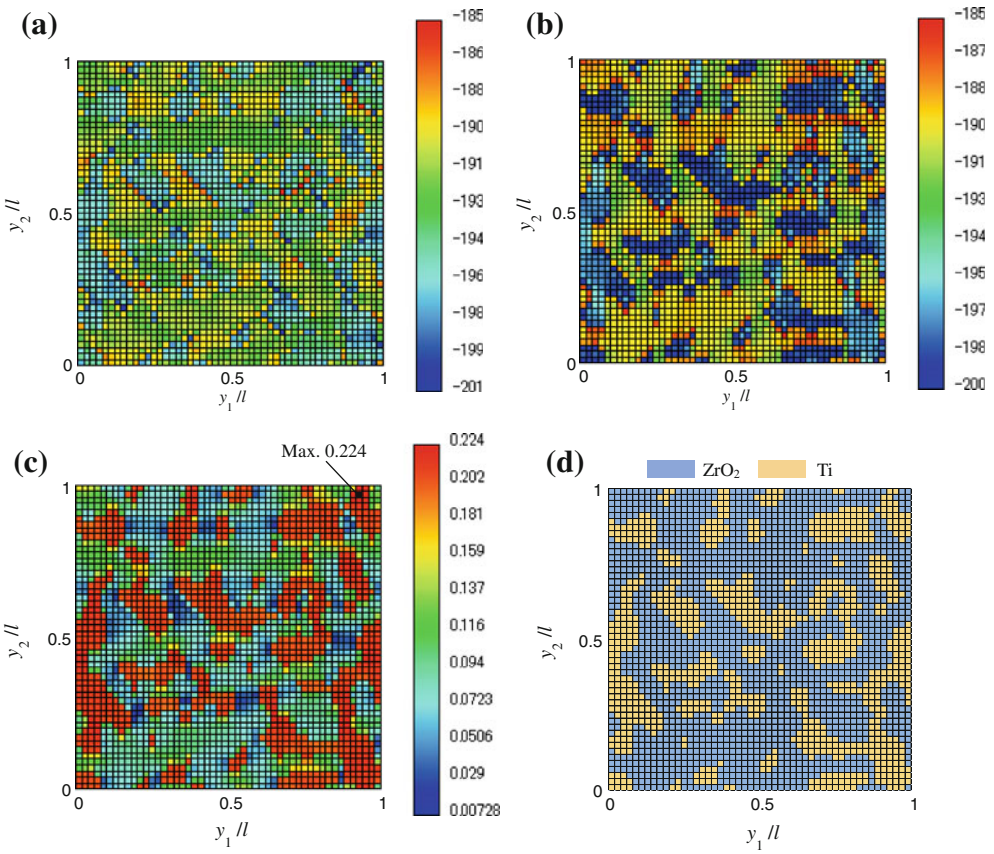

Fig. 11 Contour plots of **a** microstress σ_{22} in MPa, **b** microstress σ_{33} in MPa, **c** microscopic safety index, G, over the microstructure at the critical location $x_1/\tau = 0.9$ in the 9th layer, and **d** microstructural morphology for the 9th layer, for a functionally graded plate with realistic microstructures

constituent materials at the respective layers are chosen as design variables. The objective function is based on phase-specific failure criteria applied to an existing direct micromechanical failure analysis of FGMs.

Numerical calculations are performed for a functionally graded titanium/zirconia infinite plate that can be considered to be transversely isotropic at the macroscopic level, which is subjected to a constant temperature load on its surfaces. The functionally graded plate is assumed to possess fairly simple microstructural morphologies or random two-phase microstructures that resemble morphologies of actual FGMs for thermal stress relaxation. For comparison purposes, we also performed the conventional optimisation of the material composition distribution using simple mean-field homogenisation techniques, which does not require the computation of the microscopic stress state. The effects of the presence or absence of information about the microstructural morphology and microstresses of FGMs on the obtained optimum material composition distribution have been investigated. Numerical results demonstrate that optimisation with the knowledge of specific microstresses in FGMs results in not only a different trend of material composition distribution but also a different critical location for material failure from those obtained by optimisation without the knowledge of microstresses.

Acknowledgments This work was financially supported by KAKENHI (20923010: Grant-in-Aid for Encouragement of Scientists).

Appendix A

The macroscopic safety index $g(\mathbf{x})$ is defined as the maximum value of a stress ratio, which indicates a phase-specific failure criterion, computed over the entire domain of the RME corresponding to a macroscopic location of interest $\mathbf{x}$; with the microscopic safety index $G(\mathbf{x},\mathbf{y})$, it is expressed as follows [8,19]:

$$g(\mathbf{x}) = \max_{\mathbf{y}\in Y} G(\mathbf{x}, \mathbf{y}), \tag{A1}$$

in which

$$G(\mathbf{x}, \mathbf{y}) = \begin{cases} \frac{\sigma_{\text{eq}}(\mathbf{x},\mathbf{y})}{\sigma_{\text{y}}} & \text{if } \mathbf{y} \in Y_{\text{m}} \\ \frac{\tilde{\sigma}(\mathbf{x},\mathbf{y})}{\sigma_{\text{ut}}} & \text{if } \mathbf{y} \in Y_{\text{c}} \end{cases}, \tag{A2}$$

$$\tilde{\sigma}(\mathbf{x}, \mathbf{y}) = \max(C_1, C_2, C_3, \sigma_1, \sigma_2, \sigma_3), \tag{A3}$$

$$C_1(\mathbf{x}, \mathbf{y}) = \frac{1}{2}\left[|\sigma_1 - \sigma_2| + \frac{|\sigma_{\text{uc}}| - 2\sigma_{\text{ut}}}{|\sigma_{\text{uc}}|}(\sigma_1 + \sigma_2)\right], \tag{A4}$$

$$C_2(\mathbf{x}, \mathbf{y}) = \frac{1}{2}\left[|\sigma_2 - \sigma_3| + \frac{|\sigma_{\text{uc}}| - 2\sigma_{\text{ut}}}{|\sigma_{\text{uc}}|}(\sigma_2 + \sigma_3)\right], \tag{A5}$$

$$C_3(\mathbf{x}, \mathbf{y}) = \frac{1}{2}\left[|\sigma_3 - \sigma_1| + \frac{|\sigma_{\text{uc}}| - 2\sigma_{\text{ut}}}{|\sigma_{\text{uc}}|}(\sigma_3 + \sigma_1)\right]. \tag{A6}$$

In the above equations, σ_{eq} is the Mises equivalent stress at the microscale, σ_{y} is the yield strength of the metal phase, Y_{m} and Y_{c} denote the regions in the RME, which are composed of metal or ceramic phases, respectively; σ_{ut} and σ_{uc} are the ultimate tensile and compressive strengths of the ceramic phase, respectively; and $\sigma_i (i = 1, 2, 3)$ are the principal stresses obtained from the microstresses. Equation (A2) represents the usage of the Mises failure criterion for the metal phases and a modified-Mohr criterion for the ceramic phases.

Appendix B

An optimisation of the material composition of the functionally graded plate that does not include information on the specific microstructure is explained here. In this framework, the effective material properties of the transversely isotropic functionally graded plate are estimated by the various methods listed in Table 3. All the methods listed are mean-field homogenisation schemes for unidirectional fibrous composite materials.

For the objective function f to be minimised in the optimisation computation, the maximum value of a local safety factor s proposed by Ootao et al. [17], i.e.

$$f(\mathbf{V}) = \max_{\mathbf{x}\in\Omega} s(\mathbf{x}), \tag{B1}$$

$$s(\mathbf{x}) = \begin{cases} \frac{\bar{\sigma}_{\text{eq}}(\mathbf{x})}{\sigma_{\text{Bt}}(\mathbf{x})} & \text{if } \bar{\sigma}_{\text{m}}(\mathbf{x}) \geq 0, \\ \frac{\bar{\sigma}_{\text{eq}}(\mathbf{x})}{\sigma_{\text{Bc}}(\mathbf{x})} & \text{if } \bar{\sigma}_{\text{m}}(\mathbf{x}) < 0, \end{cases} \tag{B2}$$

is used from the viewpoint of macroscopic material failure, where $\bar{\sigma}_{\text{eq}}$ and $\bar{\sigma}_{\text{m}}$ are the Mises equivalent stress and mean normal stress at the macroscale, respectively. For the present model problem, they are expressed as follows:

$$\bar{\sigma}_{\text{eq}} = \sqrt{\bar{\sigma}_{22}^2 - \bar{\sigma}_{22}\bar{\sigma}_{33} + \bar{\sigma}_{33}^2}, \quad \bar{\sigma}_{\text{m}} = \frac{\bar{\sigma}_{22} + \bar{\sigma}_{33}}{3}, \tag{B3}$$

Table 3 Mean-field homogenisation schemes used for estimating the effective material properties of FGMs

Material property	Adopted scheme
K_{11}	Hasselman–Johnson[a] [27] and fuzzy inference[24]
E_{22}	Halpin–Tsai[b] [28] and fuzzy inference [24]
E_{33}	Linear rule of mixtures
ν_{23}, ν_{32}	Linear rule of mixtures
α_{22}	Schapery's transverse CTE model [23] and fuzzy inference [24]
α_{33}	Schapery's axial CTE model [23] and fuzzy inference [24]

[a] Infinite interfacial conductance is assumed
[b] A reinforcement parameter of $\zeta = 2$ has been used

where $\bar{\sigma}_{22}$ and $\bar{\sigma}_{33}$ are given by Eq. (23). Moreover, σ_{Bt} and σ_{Bc} are the effective strengths of the functionally graded plate to tensile and compressive stresses, respectively. After Ootao et al. [17] and Na et al. [26], the effective strengths are simply estimated by the linear rule of mixtures as

$$\sigma_{\mathrm{Bt}}(\mathbf{x}) = \sigma_{\mathrm{y}} V_{\mathrm{Metal}}(\mathbf{x}) + \sigma_{\mathrm{ut}} V_{\mathrm{Ceramic}}(\mathbf{x}), \quad \sigma_{\mathrm{Bc}}(\mathbf{x}) = \sigma_{\mathrm{y}} V_{\mathrm{Metal}}(\mathbf{x}) + |\sigma_{\mathrm{uc}}| V_{\mathrm{Ceramic}}(\mathbf{x}). \tag{B4}$$

In the implementation, the values of s are calculated at 11 discrete locations with equal intervals in each layer of the 10-layer system into which the original functionally graded plate is converted, and the maximum of those values calculated in all the layers is regarded as the value of the objective function f.

References

1. Miyamoto, Y., Kaysser, W.A., Rabin, B.H., Kawasaki, A., Ford, R.G.: Functionally Graded Materials: Design, Processing and Applications. Kluwer, Boston (1999)
2. Watanabe, R., Takahashi, H., Tamura, M., Shiota, K., Yoshida, T., Kurino, T. (eds.): Functionally Gradient Materials. Kogyo Chosakai, Tokyo (1993)
3. Wang, M., Pan, N.: Predictions of effective physical properties of complex multiphase materials. Mater. Sci. Eng. R Rep. **63**, 1–30 (2008)
4. Chen, B., Tong, L.: Thermomechanically coupled sensitivity analysis and design optimization of functionally graded materials. Comput. Methods Appl. Mech. Eng. **194**, 1891–1911 (2005)
5. Bobaru, F.: Designing optimal volume fractions for functionally graded materials with temperature-dependent material properties. Trans. ASME J. Appl. Mech. **74**, 861–874 (2007)
6. Vel, S.S., Pelletier, J.L.: Multi-objective optimization of functionally graded thick shells for thermal loading. Compos. Struct. **81**, 386–400 (2007)
7. Boussaa, D.: Optimization of temperature-dependent functionally graded material bodies. Comput. Methods Appl. Mech. Eng. **198**, 2827–2838 (2009)
8. Goupee, A.J., Vel, S.S.: Transient multiscale thermoelastic analysis of functionally graded materials. Compos. Struct. **92**, 1372–1390 (2010)
9. Pindera, M.J., Aboudi, J., Arnold, S.M.: Thermomechanical analysis of functionally graded thermal barrier coatings with different microstructural scales. J. Am. Ceram. Soc. **81**, 1525–1536 (1998)
10. Dao, M., Gu, P., Maewal, A., Asaro, R.J.: A micromechanical study of residual stresses in functionally graded materials. Acta Mater. **45**, 3265–3276 (1997)
11. Tsukamoto, H.: Analytical method of inelastic thermal stresses in a functionally graded material plate by a combination of micro- and macromechanical approaches. Compos. B Eng. **34**, 561–568 (2003)
12. Khan, K.A., Muliana, A.H.: A multi-scale model for coupled heat conduction and deformations of viscoelastic functionally graded materials. Compos. B Eng. **40**, 511–521 (2009)
13. Cannillo, V., Montorsi, M., Siligardi, C., Sola, A., de Portu, G., Micele, L., Pezzotti, G.: Microscale computational simulation and experimental measurement of thermal residual stresses in glass-alumina functionally graded materials. J. Eur. Ceram. Soc. **26**, 1411–1419 (2006)
14. Vena, P.: Thermal residual stresses in graded ceramic composites: a microscopic computational model versus homogenized models. Meccanica **40**, 163–179 (2005)
15. Terada, K., Hori, M., Kyoya, T., Kikuchi, N.: Simulation of the multi-scale convergence in computational homogenization approaches. Int. J. Solid Struct. **37**, 2285–2311 (2000)
16. Takano, N., Zako, M.: Integrated design of graded microstructures of heterogeneous materials. Arch. Appl. Mech. **70**, 585–596 (2000)
17. Ootao, Y., Tanigawa, Y., Ishimaru, O.: Optimization of material composition of functionally graded plate for thermal stress relaxation using a genetic algorithm. J. Therm. Stress. **23**, 257–271 (2000)
18. Xianfan, C., Shutian, L.: Topology description function based method for material design. Acta Mechanica Solida Sinica **19**, 95–102 (2006)
19. Goupee, A.J., Vel, S.S.: Multiscale thermoelastic analysis of random heterogeneous materials: Part II: Direct micromechanical failure analysis and multiscale simulations. Comput. Mater. Sci. **48**, 39–53 (2010)
20. Vel, S.S., Goupee, A.J.: Multiscale thermoelastic analysis of random heterogeneous materials: Part I: Microstructure characterization and homogenization of material properties. Comput. Mater. Sci. **48**, 22–38 (2010)
21. Gurdal, Z., Haftka, R.T., Hajela, P.: Design and Optimization of Laminated Composite Materials. Wiley, New York (1999)
22. Shabana, Y.M., Noda, N.: Numerical evaluation of the thermomechanical effective properties of a functionally graded material using the homogenization method. Int. J. Solid Struct. **45**, 3494–3506 (2008)
23. Schapery, R.A.: Thermal expansion coefficients of composite materials based on energy principles. J. Compos. Mater. **2**, 380–404 (1968)
24. Tanaka, K., Watanabe, H., Sugano, Y., Poterasu, V.F.: A multicriterial material tailoring of a hollow cylinder in functionally gradient materials: Scheme to global reduction of thermoelastic stresses. Comput. Methods Appl. Mech. Eng. **135**, 369–380 (1996)
25. Guinovart-Diaz, R., Bravo-Castillero, J., Rodriguez-Ramos, R., Martinez-Rosado, R., Serrania, F., Navarrete, M.: Modeling of elastic transversely isotropic composite using the asymptotic homogenization method. Some comparisons with other models. Mater. Lett. **56**, 889–894 (2002)

26. Na, K.S., Kim, J.H.: Optimization of volume fractions for functionally graded panels considering stress and critical temperature. Compos. Struct. **89**, 509–516 (2009)
27. Hasselman, D.P.H., Johnson, L.F.: Effective thermal conductivity of composites with interfacial thermal barrier resistance. J. Compos. Mater. **21**, 508–515 (1987)
28. Halpin, J.C., Tsai, S.W.: Effects of environmental factors on composite materials. Report AFML-TR 67, 423 (1969)